

Journal of Materials Chemistry A

Materials for energy and sustainability

Accepted Manuscript

This article can be cited before page numbers have been issued, to do this please use: M. Joy, B. Bloom, K. Govindaraj, J. A. Albro, A. Vadakkayil and D. H. Waldeck, *J. Mater. Chem. A*, 2025, DOI: 10.1039/D5TA04850H.



This is an Accepted Manuscript, which has been through the Royal Society of Chemistry peer review process and has been accepted for publication.

Accepted Manuscripts are published online shortly after acceptance, before technical editing, formatting and proof reading. Using this free service, authors can make their results available to the community, in citable form, before we publish the edited article. We will replace this Accepted Manuscript with the edited and formatted Advance Article as soon as it is available.

You can find more information about Accepted Manuscripts in the [Information for Authors](#).

Please note that technical editing may introduce minor changes to the text and/or graphics, which may alter content. The journal's standard [Terms & Conditions](#) and the [Ethical guidelines](#) still apply. In no event shall the Royal Society of Chemistry be held responsible for any errors or omissions in this Accepted Manuscript or any consequences arising from the use of any information it contains.

[Type here]

View Article Online
DOI: 10.1039/D5TA04850H

Development of a spin selective electrocatalyst platform and its use to study spin-polarization and d-orbital occupancy effects in oxygen evolution reaction electrocatalysts.

Received 00th January 20xx,
Accepted 00th January 20xx

DOI: 10.1039/x0xx00000x

Meera Joy,^a Brian P. Bloom,^a Keerthana Govindaraj,^a Joseph A. Albro,^a Aravind Vadakkayil,^a and David H. Waldeck^{*a}

We describe a polymer-catalyst platform that uses spin-polarized electron currents, recently reported to improve the efficiency of the oxygen evolution reaction (OER), in combination with transition metal-oxide catalysts to enhance the efficiency of their OER electrocatalysis. We describe the creation of an electrode coated with a chiral conjugated polymer film which acts as a spin transport layer and ensures that the anodic reaction proceeds with a spin bias. Systematic studies on a series of transition metal oxide catalysts demonstrate that spin selectivity improves catalytic efficiency irrespective of the catalyst's position on a 'volcano' plot and that the benefit correlates with the expected number of unpaired d-orbital electrons in the catalyst. These studies demonstrate a promising electrode scaffold for investigating the role of electron spin currents in chemical reactions.

1. Introduction

The oxygen evolution reaction (OER) is an important bottleneck for energy storage devices such as metal air batteries, water electrolysis, and regenerative fuel cells.^{1, 2} It is a limiting reaction in the process of generating molecular oxygen through redox chemistry, such as the oxidation of water during oxygenic photosynthesis, electrolysis of water into oxygen and hydrogen, and electrocatalytic oxygen evolution from oxides and oxoacids.³ Thus, it is important from both a fundamental perspective and for applications.⁴ The electrochemical OER proceeds through a complex set of four proton-coupled electron transfer steps, with adsorbed *OH, *O, and *OOH radical intermediates, to generate diatomic oxygen, which exists as a triplet in its ground state.^{5, 6}

To rationalize the activity of electrocatalysts in a family of catalyst materials, researchers often adopt Sabatier's principle, *i.e.* the notion that the binding energy of reaction intermediates should be neither too strong nor too weak to facilitate a reaction.⁷ In the case of OER this is reflected in the binding energies of oxo and hydroxyl intermediates ($\Delta G_{\text{O}} - \Delta G_{\text{OH}}$) and manifests as a 'volcano plot', in which the apex of the plot is the voltage nearest to the ideal thermodynamic potential for catalysis; *i.e.*, smallest overpotential.⁸ ⁹ In addition to this energy effect, researchers have demonstrated that electrocatalytic activity is impacted by electron orbital and spin effects, *e.g.* engineering e_g electron filling in LaCoO_3 -based electrocatalysts,¹⁰ regulating e_g electron filling and spin states through sulfur¹¹ and fluorine¹² atom doping, and Zn^{2+} substitution in spinel Co_3O_4 catalysts.¹³

While considerable progress has been made using these approaches, recent studies demonstrate that spin polarizing reaction intermediates during OER can also improve catalytic activity. Spin polarization during catalysis has been achieved primarily through two approaches: 1) application of an external magnetic field on a paramagnetic or ferromagnetic catalyst^{14,19,20,21} and 2) use of chiral catalysts that display the chiral-induced spin selectivity (CISS) effect.^{22,26} The CISS effect has been used in a number of different ways to boost OER efficiency,^{27,32} including (photo-) electrocatalytic water splitting, in which covering the anode with chiral molecules increases the overall cell performance.^{33,35} Note, that other methods for spin-polarizing electron currents during OER have also been explored, including the implementation of 'spin-pinning' layers or spin-polarized defect sites, the exploitation of spin-selective carrier transport, and the introduction of a chiral bias using molecular additives, among others; however these methods are less well studied.^{15,36,40} The spin-polarization enhanced OER is often attributed to changes in the transition state energies of reaction intermediates, as well as reaction pathways, compared to systems with unpolarized catalysts.^{14, 15, 16} Both the strength of an applied external magnetic field on a ferromagnetic catalyst and the 'degree of chiral imprinting' on a chiral catalyst can affect the magnitude of spin polarization and consequently the improvement in OER performance.^{41, 42} While a large breadth of studies demonstrate that spin polarization enhances OER,⁴³ a thorough understanding of how these effects coincide, or not, with traditional methods for predicting catalyst activity, *i.e.*, 'volcano' plots, is unknown.

This work distinguishes the effect of the spin-polarized current from other contributions to catalytic activity by performing a systematic study in which the same spin polarization is transferred to different catalysts. To this end, we developed a chiral scaffold that delivers spin-polarized electron currents to OER catalysts and probe the impact of spin polarization on a series of achiral metal-oxide catalysts. Note this is operationally a similar approach to that

^a Chemistry Department, University of Pittsburgh, Pittsburgh, Pennsylvania 15260, United States

*Supplementary Information available: [details of any supplementary information available should be included here]. See DOI: 10.1039/x0xx00000x



reported previously using chiral helices with Ni,⁴⁰ however here we use polyaniline (PANI) as a robust and conductive chiral scaffold. This approach circumvents the need to create ferromagnetic catalysts or chiral catalysts, rather the same catalyst can be studied both with and without spin-polarizing electron currents.

Previous studies have shown that PANI operates as a successful catalyst support for chemical reactions^{44,46} and, when made chiral using dopants, functions as an efficient spin filter.^{47,49} By combining these two attributes, we demonstrate the fabrication of a flexible catalyst support platform that: 1) can incorporate a wide array of metal catalysts through drop casting nanoparticles or through electrodeposition,^{50,53} to form PANI-catalyst composites and 2) owing to the robust pH and potential stability of PANI, is capable of operating under basic and acidic conditions at both high anodic and cathodic potentials. Because the chiral polyaniline thin film is placed between the catalyst and the anode, it serves as a 'spin transport layer', i.e. it abstracts (transmits) spin-polarized electrons from (to) the electrocatalyst thereby leading to spin alignment of reaction intermediates on the catalyst surface. Note that, the emergence of spin-polarized electron transport through the chiral polyaniline does not rely on magnetic properties of the catalyst. Previous studies have shown that chiral molecules, materials, and their assemblies, can manifest CISS without external magnetic components or magnetic fields.^{54,55,56}

Below we apply this unique platform to examine how the OER activity of simple transition-metal oxide catalysts changes on spin-polarizing (chiral) polyaniline films versus on nonspin-polarizing (racemic) polyaniline films. Our findings show that the spin-polarizing catalyst scaffold improves OER activity and implies that spin acts as an additional design feature that operates in concert with traditional activity metrics, e.g. volcano plots. While the focus of the studies herein is on OER, the versatility of the chiral PANI-catalyst support represents a viable system for studying the effect of spin in other chemical reactions.

2. Experimental Section

2.1. Materials

All commercial materials and solvents were used without further purification unless otherwise indicated. Sodium borohydride, Nafion perfluorinated resin solution, S- camphor sulfonic acid, R-camphor sulfonic acid, p-phenylene diamine, aniline, nickel (II) sulfate hexahydrate, iron (II) sulfate heptahydrate, copper (II) sulfate pentahydrate, cobalt (II) sulfate heptahydrate, iridium (IV) oxide, ruthenium (IV) oxide, titanium (IV) oxide, sodium perchlorate monohydrate and urea were purchased from Sigma-Aldrich. HCl was purchased from Fischer chemicals. KOH, H₂SO₄ were purchased from Fisher Scientific. Sodium nitrite and boric acid were purchased from J.T. Baker and Fisher Bio-Reagents respectively.

2.2. Preparation of spin transport layer

Substrates were fabricated by e-Beam deposition of 3 nm Ti and 10 nm Au onto quartz substrates, using a Plasma-Electron Beam Evaporator MEB550S. The polyaniline film was then prepared by two sequential steps: covalent modification of an electrode through grafting, followed by electropolymerization of aniline. To ensure the stability of the chiral support, the electrode surface was molecularly grafted, following a previously published procedure,⁵⁷ through an *in-situ* generated diazonium salt. The 4-aminophenyl diazonium salt was formed by reacting 5mM p-phenylene diamine with 1 equivalent of sodium nitrite in a 0.5 M HCl solution. Reduction of the salt under moderate potentials (-0.4 V vs Ag/AgCl) formed a metal-carbide bond and the grafted electrode was then sonicated for 5 minutes to remove any unbound molecules. The resulting amine-terminated modified electrode surface now acts as an initiation site for the polymerization of aniline.⁵⁸ Electropolymerization of aniline was performed in the presence of R- or S-camphor sulfonic acid (CSA), a counterion which binds to the backbone of the polymer, to form chiral R- PANI or S-PANI. Conversely, polymerization in the presence of racemic CSA resulted in no net chirality of the result polymer, i.e. a null response in the circular dichroism was observed. The PANI layer was prepared through electropolymerization in a 0.2 M aniline and 1 M S-, R-, or rac-CSA solution under potentiostatic conditions (0.75 V) until the desired thickness (*ca.* 100-120 nm) was achieved.

2.3. Electrodeposition of metal electrocatalysts

The electropolymerized films were de-doped by immersing them in 0.5 M ammonium hydroxide solution for 20 minutes and then thoroughly rinsing with deionized water. Catalysts were then deposited onto the PANI films through electrodeposition. For Ni catalysts,⁵⁹ a solution of 0.01 M nickel (II) sulfate hexahydrate in 0.01 M boric acid and 1 x 10⁻⁶ M H₂SO₄ at -1.4 V vs Ag|AgCl for 25 seconds was used. For Co catalysts,⁵⁹ a solution of 0.01 M cobalt (II) sulfate heptahydrate in 0.01 M boric acid and 1 x 10⁻⁶ M H₂SO₄ at -1.4 V vs Ag|AgCl for 25 seconds was used. For Fe catalysts, a solution of 0.01 M iron (II) sulfate heptahydrate in 0.01 M boric acid and 1 x 10⁻⁶ M H₂SO₄ at -1.4 V vs Ag|AgCl for 25 seconds was used. For Cu catalysts,⁶⁰ a solution of 0.01 M copper (II) sulfate pentahydrate and 0.1 M sodium perchlorate monohydrate at -1.2 V vs Ag/AgCl for 25 seconds was used.

2.4. Preparation of catalyst ink solutions

IrO₂ and RuO₂ ink solutions were prepared in 10 µL of 5 wt % Nafion and 1 mL of a water/ethanol solution (1:1 v/v). The mixture was sonicated for 15 minutes and then 5 mg of the catalyst was added to the solution. An additional 30 min of sonication was performed and a 2 µL aliquot of the solution was drop cast onto 0.07 cm² glassy carbon electrode coated with the PANI film. The TiO₂ ink solution was prepared by sonicating 3 mg of TiO₂ in 30µL of 5 wt% Nafion and 1 mL of a water/ethanol solution (3:1 v/v) for 30 minutes.

2.5. Characterization



Circular dichroism measurements were performed using a Jasco J810 CD spectrometer with an integration time of 4 s and a bandwidth of 1 nm. UV-Visible absorbance measurements were made using an Agilent (Model 8453) spectrometer. X-ray photoelectron

tip, followed by ~60 different regions with a South magnetized tip, and then lastly another ~60 regions with a North magnetized tip. Only data in which the first North magnetized tip is within the 95% confidence interval of the second North magnetized tip

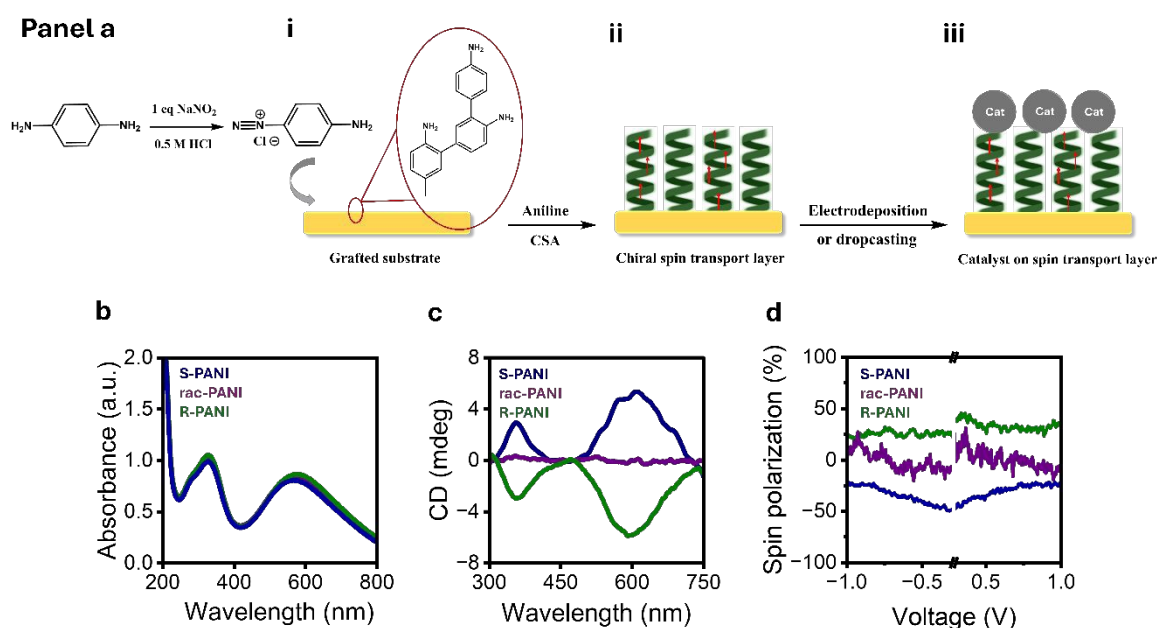


Figure 1. Panel a shows a schematic diagram for the preparation of chiral polyaniline spin transport layers by electropolymerization on a chemically derivatized substrate: i. a diazonium salt was generated *in situ* and its reduction on the surface of electrode forms a metal-carbide bond, ii. electropolymerization of aniline onto the chemically derivatized electrode surface in the presence of camphor sulfonic acid was used to produce a chiral polyaniline film, and iii. the OER electrocatalyst material was deposited on the chiral polymer film, either by electrodeposition or by drop casting. Absorbance (b) and circular dichroism spectra (c) of electropolymerized S-PANI (blue), R-PANI (green), and rac-PANI (purple) films. Spin polarization (d) of S- (blue), R- (green), and rac-PANI (purple) films were determined using mcAFM as a function of applied voltage

spectroscopy (XPS) measurements were performed using a PHI Genesis system at a 55 eV pass energy, 20 ms dwell time, and with a 0.1 eV increment. All of the data were charge referenced to the c-c peak of adventitious carbon, 284.8 eV. SEM images were collected on a ZEISS Sigma 500 VP scanning electron microscope (SEM at a working distance of 3-6 mm and an accelerating voltage of 3 kV. The mc-AFM measurements were carried out on a Bruker Dimension Icon atomic force microscope. The PANI films were electrodeposited on 100 nm Au/5 nm Ti/Si wafer. To ensure that the thickness of the electrodeposited film was the same for R- and S-PANI films, surface profilometer measurements (KLA-Tencor Alpha-Step IQ Surface Profiler) were performed following electropolymerization. To decrease surface roughness effects, which can arise with thicker films, thinner PANI films were used to perform the mcAFM measurements; the average thickness of R-PANI films (14.1 ± 2.2 nm), S-PANI (12.9 ± 2.7 nm), and rac-PANI films (12.7 ± 2.3 nm) were within error of each other. The mc-AFM measurements were performed using a ferromagnetic CoCr tip (HQ:NSC18/Co-Cr, MikroMasch) with a force constant of 2.8 N/m. The ferromagnetic AFM probes were magnetized by placing the AFM probe (tip apex facing upwards) onto the corresponding pole of a magnet. Measurements were made by collecting current-voltage (*I-V*) curves at different regions of the film (c.a. 60 spots) for a North magnetized

measurement were considered viable.

2.6. Electrochemical Measurements

Electrochemical measurements were carried out using either a 618 B or 430 A potentiostat (CH Instruments). The reference electrode was a saturated KCl Ag|AgCl (CH Instruments) and the counter electrode was a platinum wire. Linear sweep voltammetry (LSV) experiments for all of the catalyst materials were collected at a scan rate of 10 mV s⁻¹. The electrochemical results reported in this work were all *iR* compensated.

3. Results and Discussion

3.1. Deposition and characterization of polyaniline spin transport layer

To form catalyst-coated polyaniline thin films, a three-step process was used; see Figure 1 for a schematic of the process. Briefly, bi-/tri-layer polymer nucleation sites were first chemically grafted onto the electrode surface through reduction of an *in situ* generated diazonium salt (i). See Supplementary Information for characterization of the grafted surface. Next, aniline was electropolymerized onto the electrode (ii). Figure 1b shows



representative absorbance spectra of PANI films prepared in the presence of S-camphorsulfonic acid (S-PANI, blue), R-camphorsulfonic acid (R-PANI, green), and racemic-camphorsulfonic acid (rac-PANI, purple). The spectral features at 330 nm and 590 nm are characteristic of the emeraldine base form of polyaniline and have previously been assigned to a benzenoid π - π^* transition and the quinoid groups in the polymer backbone, respectively.⁶¹ Films of thickness ranging from 80-100 nm were used for the experiments, and the thickness was controlled through the polymerization time. A calibration curve for determining the thickness from the absorbance is shown in Figure S2. In the presence of chiral camphorsulfonic acid dopants, the films manifest chiroptical properties consistent with that shown in other works.⁶² Figure 1c shows corresponding circular dichroism spectra of the resulting S-PANI (blue) and R-PANI thin films (green) in which mirror image Cotton effects are observed at the electronic transitions of the polymer, indicating successful chirality induction in the films prepared with chiral dopants. Conversely, a null circular dichroism response was observed for the rac-PANI (purple).

To demonstrate that chiral PANI thin films act as spin transport layers, magnetic conductive atomic force microscopy (mcAFM) was performed using a magnetized ferromagnetic AFM tip. Because of the CISS effect, the conduction of charge current is favored for one electron spin orientation, *i.e.* tip magnetization, over that of the other.^{63, 64} Figure S3 shows average *I*-*V* curves measured for R-, S-, and rac-PANI with a South and North magnetized ferromagnetic AFM tip. For S-PANI films a higher current is observed when the electron spin is aligned antiparallel to its momentum whereas the opposite is observed for R-PANI films, a higher current is observed when the

electron spin is aligned parallel to its momentum. Conversely, for rac-PANI no difference in *I*-*V* response with magnetization was observed. The asymmetry in current response was used to obtain a spin polarization $\frac{I_{\text{parallel}} - I_{\text{antiparallel}}}{I_{\text{parallel}} + I_{\text{antiparallel}}} * 100\%$ and the data are plotted in Figure 1d as a function of applied bias. The equal and opposite average spin polarization for S-PANI ($-34.66 \pm 9.5\%$) and R-PANI ($30.52 \pm 8.7\%$) is a hallmark of the CISS effect. Note, the spin polarization values observed in this work are in reasonable agreement with other literature reports for chiral PANI.^{47, 48, 49}

3.2. Oxygen evolution reaction with electrodeposited catalysts

Next, we compared the OER activity of catalysts deposited on R- and S-PANI thin films, which spin polarize charge currents, to rac-PANI thin films, which do not. Two main methods were used for deposition of the catalysts (step iii in Figure 1a): (1) electrodeposition of catalyst nanoparticles onto the PANI films, and (2) drop casting of commercially available nanoparticle catalysts. Details of catalyst preparation are provided in the Experimental section. Initial studies investigated nickel, iron, cobalt, and copper catalysts formed from an acidic metal salt solution under reductive potentials (see Experimental section for detailed procedures). Figure S4 shows that the chiro-optical properties of the underlying PANI layer persist through the electrodeposition and OER electrolysis. Note that, X-ray photoelectron spectra (XPS) (Figure S5 and S6) show that the electrodeposited material is fundamentally equivalent when deposited on R-, S-, and rac-PANI; *i.e.*, the elemental composition and oxidation state distribution of the metals are within error of each other. In addition, scanning electron micrographs (Figure S7) indicate

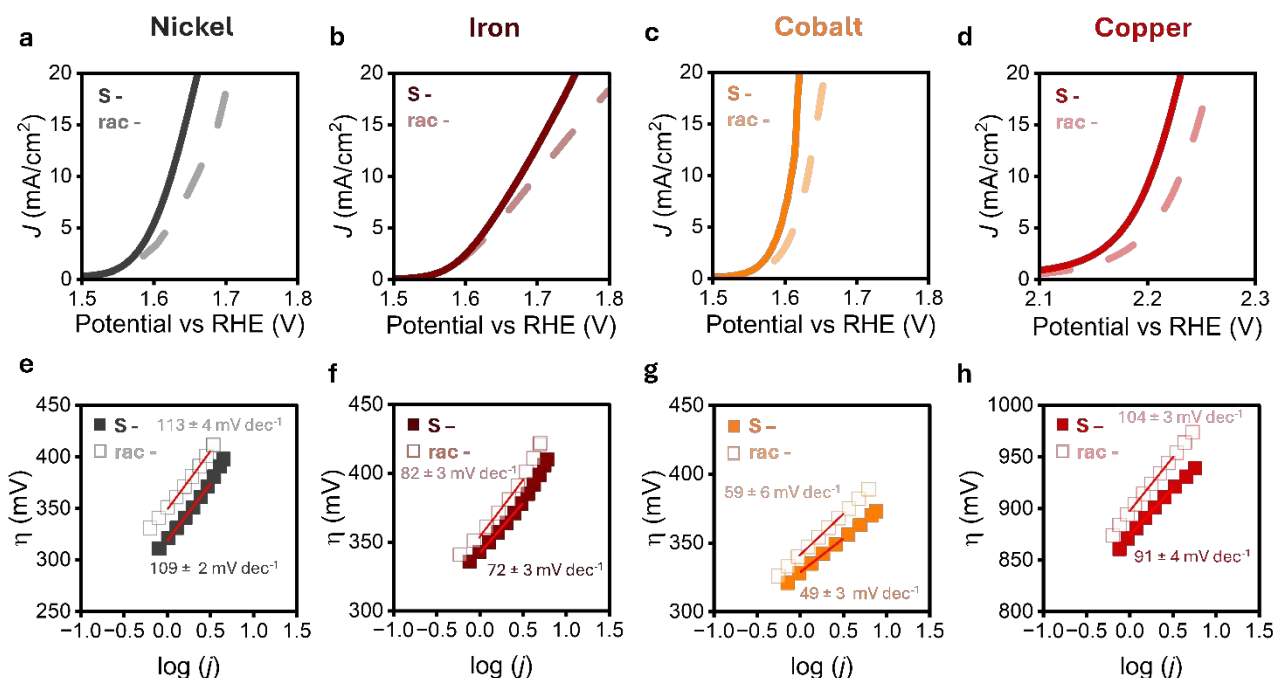


Figure 2. Panels a-d show linear sweep voltammograms of nickel (grey), iron (brown), cobalt (orange) and copper (red) based metal-oxide catalysts electrodeposited on S-PANI (solid line) and rac-PANI (dotted line). These data represent the average of three separately prepared electrodes. Panels e-h show corresponding Tafel plots of the catalysts deposited on S-PANI (filled squares) and rac-PANI films (open squares). These data represent the average from three separately prepared electrodes and the error in slope is associated with the standard deviation of the mean.



that the catalyst size and morphology are also similar. These characterization data imply that the morphological features and composition of the catalyst nanoparticles do not depend on whether the underlying PANI layer is chiral or racemic.

nanoparticle catalysts, namely IrO_2 and RuO_2 on chiral PANI thin films over *rac*-PANI films. Figures 3a & b show linear sweep voltammograms that display a decrease in reaction overpotential of catalysts deposited on S-PANI (solid line) compared to *rac*-PANI films (dashed line), and Figures 3d & e show a decrease in the Tafel slope

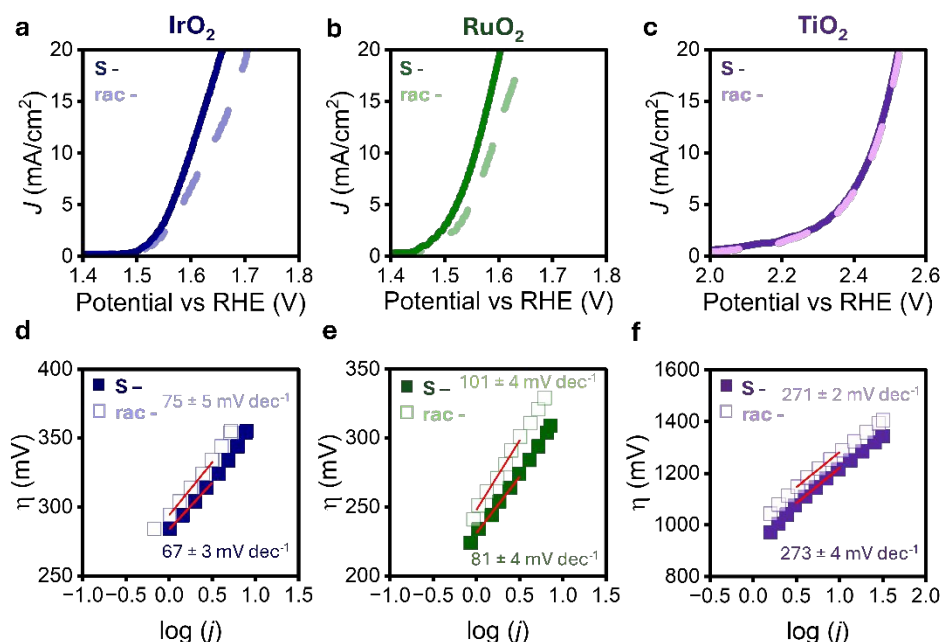


Figure 3. a-c shows the linear sweep voltammograms of IrO_2 (blue), RuO_2 (green), and TiO_2 (purple) nanoparticle catalysts in Nafion drop cast onto chiral S-PANI (solid line) and achiral *rac*-PANI (dashed line) in a 1M KOH electrolyte. These data represent the average of three separately prepared electrodes. Panels d-f show Tafel plots and corresponding slopes for IrO_2 (blue), RuO_2 (green), and TiO_2 (purple) drop cast onto chiral (filled symbol) and racemic (open symbol) PANI films. These data represent the average from three separately prepared electrodes and the error in slope is associated with the standard deviation of the mean.

Figures 2 a-d show linear sweep voltammograms, under potential conditions at which OER occurs, for nickel (grey), iron (brown), cobalt (orange), and copper (red) based metal-oxide catalysts deposited on *rac*-PANI (dashed line) and S-PANI (solid line) thin films. For each catalyst type a decrease in the reaction overpotential, η , is observed on S-PANI thin films compared to *rac*-PANI. In addition, the catalysts on the chiral S-PANI films (filled squares) show a decrease in the Tafel slope compared to the same catalysts on the *rac*-PANI films (open squares); see Figure 2 e-h. Note that measurements on catalysts deposited on R-PANI thin films exhibit similar catalytic behavior to that of S-PANI thin films and are shown in Figures S8-S10. Collectively, these data demonstrate that catalysts placed on thin film scaffolds that spin-filter charge current, i.e. chiral PANI, exhibit improved OER kinetics compared to films which do not spin-filter the electron current, *rac*-PANI. To ensure that the improved performance is not associated with changes in the electrochemical surface area double layer capacitance measurements were performed; see Figure S11 and corresponding discussion in the Supplementary Information.

3.3. Oxygen evolution reaction with commercial catalysts

A similar improvement in OER activity was also observed for drop-cast Nafion ink suspensions containing commercially available

of IrO_2 and RuO_2 catalysts deposited on S-PANI (filled squares) compared to *rac*-PANI (open squares) films. Note that, Figures S8-S10 show measurements made on R-PANI thin films in which a similar performance to S-PANI films is observed. Interestingly, measurements made using ink suspensions comprising TiO_2 catalysts did not exhibit changes, outside of statistical error, in overpotential or Tafel slope, when deposited on S-PANI films and *rac*-PANI films (see Figures 3c & f). Note that similar to the case of electrodeposited catalysts, the electrochemical surface area of drop cast ink suspensions, determined through double layer capacitance, confirms that the comparison between S-PANI and *rac*-PANI films is not influenced by differences in electrochemically active surface area (Figure S11).

3.4. Electroactive forms of explored catalysts

To understand these data, consider that the most likely forms of the catalysts are oxyhydroxides for Fe, Co, and Ni,⁶⁵ and IrO_2 , RuO_2 ,⁶⁶ CuO ,⁶⁷ and TiO_2 ⁹ for the others, under the voltage and pH conditions for the OER in this study. Note that this assignment of the catalytic form is consistent with *ab initio* calculations, as well as Pourbaix diagrams,^{68,72} and were substantiated electrochemically. For example, Figure S12 shows oxidation peaks associated with the electrochemical conversion of Ni^{2+} to Ni^{3+} for nickel-based catalysts



and Co^{2+} to Co^{3+} for cobalt-based catalysts that occur prior to OER currents. Table 1 summarizes the reaction overpotentials (η) and Tafel slopes from measurements of different catalysts on S-PANI and rac-PANI electrodes, and it compares our findings to previous measurements published in the literature, where possible. To ensure valid comparisons, we cite works that operate under similar reaction and solution conditions to that reported here. The overpotential and Tafel slope of catalysts deposited on rac-PANI are in most instances comparable to that of achiral catalysts reported in the literature and

Table 1. Comparison of the reaction overpotential, η , and Tafel slope, b , for catalysts deposited on S-PANI and rac-PANI to that published previously in the literature on the same catalysts. The data points represent the average from three independently prepared electrodes, and the error corresponds to the standard deviation from the mean.

Catalyst	S-PANI		rac-PANI		Literature		Ref.
	η (mV)	b (mV dec ⁻¹)	η (mV)	b (mV dec ⁻¹)	η (mV)	b (mV dec ⁻¹)	
NiOOH	394 ± 3	109 ± 2	429 ± 2	113 ± 4	533-620	105	65,73
FeOOH	416 ± 2	72 ± 3	449 ± 2	82 ± 3	450	68-100	65
CoOOH	380 ± 7	49 ± 3	407 ± 8	59 ± 6	370-430	69-95	74
CuO	969 ± 3	91 ± 4	1006 ± 4	104 ± 3	400-600	89-110	67, 75, 76
IrO ₂	369 ± 7	67 ± 3	402 ± 3	75 ± 5	340	93	36,77
RuO ₂	326 ± 8	81 ± 4	355 ± 7	101 ± 4	366	104	36,78
TiO ₂ *	1213 ± 5	273 ± 4	1223 ± 5	271 ± 6	1250	-	9

*Values reported at a current density of 0.1 mA cm⁻² to match the literature reported overpotential values at the given current density

3.5. Trends in spin promoted oxygen evolution reaction

To examine how spin polarization fits within the context of Sabatier's principle, we have constructed a volcano plot comprising the different catalysts investigated in this study. Figure 4a plots the experimentally determined reaction overpotential at 10 mA cm⁻² for catalysts deposited on S-PANI thin films (filled symbol) and rac-PANI films (open symbol). Note that, the free energies of the adsorbed reaction intermediates ($\Delta G_{\text{O}} - \Delta G_{\text{OH}}$) were taken from previous calculations^{9, 65, 66, 67} on catalysts of the form expected to be present during OER under these potential and pH conditions. An approximately 20-40 mV reduction in overpotential is observed for

all of the measured catalysts, with the exception of TiO₂ for which no improvement was observed. Note that the reduction in overpotential is independent of whether the catalyst is on the left or right side of the apex of the volcano plot. These findings suggest that spin alignment of reaction intermediates, imparted through a spin transport layer, is not changing the free energies of the adsorbates, but instead represents an additional control variable that can improve catalysis. Figure 4b shows an expanded view near the apex of the volcano plot, and the spin promoted shift in overpotential values is indicated by the dashed green line. Previous studies have reported that the transition state energies for different steps in the OER are strongly affected by spin alignment on the catalyst surface;^{79,}

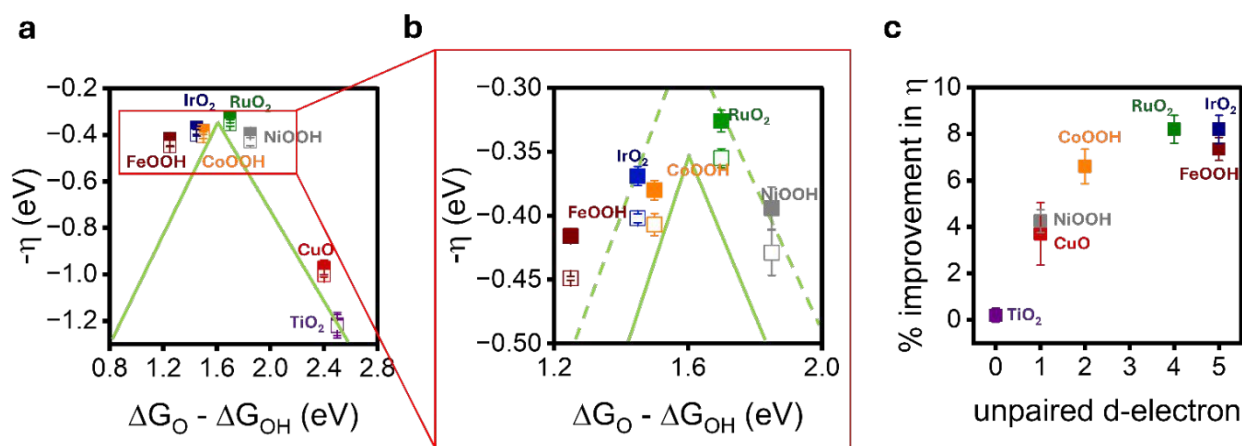


Figure 4 (a) Relationship between the OER overpotentials, η , at 10 mA cm⁻² and the difference in reaction intermediate adsorption energies, ($\Delta G_{\text{O}} - \Delta G_{\text{OH}}$), for catalysts prepared on S-PANI (filled symbols) and rac-PANI films (open symbols). The green fitted line is adapted from Ref 9. Panel (b) shows a zoomed in region near the apex of the volcano plot. Note that the free energies of the adsorbed reaction intermediates ($\Delta G_{\text{O}} - \Delta G_{\text{OH}}$) values were adapted from references 9, 59, 60, and 61 on catalysts of the form expected to be present during OER collected under the experimentally applied potential and pH conditions. Panel (c) shows the correlation between the percent improvement in reaction overpotential of S-PANI films to rac-PANI films to the number unpaired electrons in the d-orbitals of the catalyst's oxidation state formed during OER. The data points represent the average from three independently prepared electrodes, and the error bars correspond to the standard deviation to the mean.



⁸⁰ our hypothesis that selective spin injection into an electrocatalyst (because of CISS) should improve reaction efficiency, presumably by polarizing reaction intermediates and promoting the formation of triplet oxygen, is corroborated by these data. It is important to stress that the chiral spin transport layer used in this work is not the best, exhibiting a modest spin polarization of ~35 %, and that a more significant improvement would likely be observed with a better spin transport layer.

Interestingly, the percent improvement in overpotential ($(\eta_{\text{rac}} - \eta_{\text{s}})/\eta_{\text{rac}} * 100 \%$) correlates with the expected number of unpaired electrons in the catalyst's d-orbitals (Figure 4c). An increase in the number of unpaired electrons shows a more favorable response to the spin selective transport emanating from chiral PANI for improving the OER. Note that, the TiO₂ catalysts do not possess any unpaired d-orbital electrons at these pH and potential conditions, and no improvement in the OER with chiral PANI is observed. In other CISS studies researchers have shown the importance of unpaired spins in electrode materials to promote long-range spin-selective transport,^{81, 82} and it may be that a similar mechanism operates here. Concerning whether one or more of the catalyst materials becomes magnetized during the OER reaction, the data presented here is moot. Such a claim would require that the magnetization of the electrode assemblies be measured *in operando* and is beyond the scope of this work.

Conclusions

This work developed a chiral polymer scaffold as a spin-transport layer and examined its use for enhancing the performance of simple transition metal oxide catalysts in the OER reaction, which is known to be sensitive to the electron spin. We showed that use of the chiral polymer scaffolds leads to a decreased reaction overpotential and Tafel slope for the OER catalysis compared to analogous nonpolarizing (achiral) scaffolds for the same catalyst. Through investigation of a series of transition metal oxide catalysts, we showed that spin polarization can improve the reaction overpotential beyond the conventional constraints set forth by considering the adsorption energies of reaction intermediates alone. Interestingly, the OER improvement correlates with the expected number of unpaired d-electrons in the catalyst, however the cause of this correlation requires further work for full elucidation. This work demonstrates that a chiral catalyst scaffold can be used to enhance spin-dependent electrocatalysis.

Data availability

The data supporting this article has been included as part of the Supplementary Information.

Author contributions

Meera Joy: formal analysis, investigation, writing-original draft; Brian P. Bloom: XPS, SEM characterization, writing (editing and review);

Keerthana Govindaraj: mcAFM measurements; Joseph A. Albro: AFM topography imaging; Aravind Vadakkayil: Technique; David H. Waldeck: conceptualization, project administration, supervision, writing-review & editing

Conflicts of interest

The authors declare that they have no known competing financial interests or personal relationships that could have appeared to influence the work reported in this paper.

Acknowledgements

This material is based upon work supported by the Defense Advanced Research Projects Agency (DARPA) under Agreement No HR00112390110 and United States National Science Foundation (NSF) CHE-2420811.

References



- ¹ Y. J. Wang, D. P. Wilkinson, J. Zhang, *Chem. Rev.*, 2011, **111**, 7625–7651.
- ² P. Boldrin, E. Ruiz-Trejo, J. Mermelstein, J. M. Bermúdez Menéndez, T. Ramírez Reina, N. P. Brandon, *Chem. Rev.*, 2016, **116**, 13633–13684.
- ³ G. M. Whitesides, G. W. Crabtree, *Science*, 2007, **315**, 796–798.
- ⁴ N. T. Suen, S. F. Hung, Q. Quan, N. Zhang, Y. J. Xu, H. M. Chen, *Chem. Soc. Rev.*, 2017, **46**, 337–365.
- ⁵ S. Chretien, H. Metiu, *J. Chem. Phys.*, 2008, **129**, 074705.
- ⁶ H. Dau, C. Limberg, T. Reier, M. Risch, S. Roggan, P. Strassser, *Chem. Cat. Chem.*, 2010, **2**, 724–761.
- ⁷ M. Che, *Catal. Today*, 2013, **218**, 162–171.
- ⁸ J. Rossmeisl, Z. -W. Qu, H. Zhu, G. -J. Kroes, J. K. Nørskov, *J. Electroanal. Chem.*, 2007, **607**, 83–89.
- ⁹ I. C. Man, H. Y. Su, F. Calle-Vallejo, H. A. Hansen, J. I. Martínez, N. G. Inoglu, J. Kitchin, T. F. Jaramillo, J. K. Nørskov, J. Rossmeisl, *Chem. Cat. Chem.*, 2011, **3**, 1159–1165.
- ¹⁰ J. Qian, T. Wang, Z. Zhang, Y. Liu, J. Li, D. Gao, *Nano Energy*, 2020, **74**, 104948.
- ¹¹ J. Ran, T. Wang, J. Zhang, Y. Liu, C. Xu, S. Xi, D. Gao, *Chem. Mater.*, 2020, **32**, 3439–3446.
- ¹² J. Ran, L. Wang, M. Si, X. Liang, D. Gao, *Small*, 2023, **19**, 2206367.
- ¹³ R. M. Ramsundar, V. K. Pillai, P. A. Joy, *Phys. Chem. Chem. Phys.*, 2018, **20**, 29452–29461.
- ¹⁴ X. Ren, T. Wu, Y. Sun, Y. Li, G. Xian, X. Liu, C. Shen, J. Gracia, H. J. Gao, H. Yang, *Nat. Commun.*, 2021, **12**, 2608.
- ¹⁵ T. Wu, X. Ren, Y. Sun, S. Sun, G. Xian, G. G. Scherer, A. C. Fisher, D. Mandler, J. W. Ager, A. Grimaud, *Nat. Commun.*, 2021, **12**, 3634.
- ¹⁶ T. Wu, Z. J. Xu, *Curr. Opin. Electrochem.*, 2021, **30**, 100804.
- ¹⁷ X. Ren, T. Wu, Z. Gong, L. Pan, J. Meng, H. Yang, F. B. Dagbjartsdottir, A. Fisher, H. -J. Gao, Z. J. Xu, *Nat. Commun.*, 2023, **14**, 2482.
- ¹⁸ F. A. Garces-Pineda, M. Blasco-Ahicart, D. Nieto-Castro, N. Lopez, J. R. Galan-Mascaros, *Nat. Energy*, 2019, **4**, 519–525.
- ¹⁹ C. Hunt, Z. Zhang, K. Ocean, R. P. Jansonius, M. Abbas, D. J. Dvorak, A. Kurimoto, E. W. Lees, S. Ghosh, A. Turkiewicz, F. A. Garces Pineda, D. K. Fork, C. P. Berlinguette, *J. Am. Chem. Soc.*, 2022, **144**, 733–739.
- ²⁰ A. Karmakar, D. Mahendrian, R. Madhu, P. Murugan, and S. Kundu *J. Mat. Chem. A* 2023, **11**, 16349.
- ²¹ S. Nagappan, A. Karmakar, R. Madhu, S. S. Selvasundarasekar, S. Kumarevel, K. Bera, H. N. Dhandapani, D. Sarkar, S. M. Yusuf, and S. Kundu *ACS Appl. Energy Mater.* 2022, **5**, 11483.
- ²² W. Zhang, K. B. Ghosh, F. Tassinari, R. Naaman, *ACS Energy Lett.*, 2018, **3**, 2308–2313.
- ²³ S. Ghosh, B. P. Bloom, Y. Lu, D. Lamont, D. H. Waldeck, *J. Phys. Chem. C*, 2020, **124**, 22610–22618.
- ²⁴ K. B. Ghosh, W. Zhang, F. Tassinari, Y. Mastai, O. Lidor-Shalev, R. Naaman, P. Möllers, D. Nurenberg, H. Zacharias, J. Wei, *J. Phys. Chem. C*, 2019, **123**, 3024–3031.
- ²⁵ A. N. Nair, S. Fernandez, M. Marcos-Hernández, D. R. Romo, S. R. Singamaneni, D. Villagran, S. T. Sreenivasan, *Nano Lett.*, 2023, **23**, 9042–9049.
- ²⁶ A. Vadakkayil, C. Clever, K. N. Kunzler, S. Tan, B. P. Bloom, D. H. Waldeck, *Nat. Commun.*, 2023, **14**, 1067.
- ²⁷ P. K. Bhartiya, M. Srivastava, D. Mishra, *Int. J. Hydrogen Energy*, 2021, **47**, 42160–42170.
- ²⁸ J. Meng, H. Li, R. Chen, X. Sun, X. Sun, *Chem. Plus. Chem.*, 2019, **84**, 1816–1822.
- ²⁹ W. Zhang, W. Wang, Y. Hu, H. Guan, L. Hao, *Int. J. Hydrogen Energy*, 2021, **46**, 3504–3509.
- ³⁰ Y. Liang, M. Lihter, M. Lingenfelder, *Isr. J. Chem.*, 2022, **62**, e202200052.
- ³¹ P. Vensaus, Y. Liang, N. Zigon, N. Avarvari, V. Mujica, G. J. Soler-Illia, M. J. Lingenfelder, *Chem. Phys.*, 2024, **160**, 111103.
- ³² D. Barik, U. Utkarsh, K. B. Ghosh, *Chem. Commun.*, 2025, **61**, 6226–6245.
- ³³ W. Mtangi, V. Kiran, C. Fontanesi, R. Naaman, *J. Phys. Chem. Lett.*, 2015, **6**, 4916–4922.
- ³⁴ W. Mtangi, F. Tassinari, K. Vankayala, A. Vargas Jentzsch, B. Adelizzi, A. R. Palmans, C. Fontanesi, E. W. Meijer, R. Naaman, *J. Am. Chem. Soc.*, 2017, **139**, 2794–2798.
- ³⁵ F. Tassinari, K. B. Ghosh, F. Parenti, V. Kiran, A. Mucci, R. Naaman, *J. Phys. Chem. C*, 2017, **121**, 15777–15783.
- ³⁶ A. Vadakkayil, W. A. Dunlap-Shohl, M. Joy, B. P. Bloom, D. H. Waldeck, *ACS Catal.*, 2024, **14**, 17303–17309.
- ³⁷ H. Gajapathy, S. Bandaranayake, E. Hruska, A. Vadakkayil, B. P. Bloom, S. Londo, J. McClellan, J. Guo, D. Russell, F. M. de Groot, F. Yang, *Chem. Sci.*, 2024, **15**, 3300–3310.
- ³⁸ L. Pan, M. Ai, C. Huang, L. Yin, X. Liu, R. Zhang, S. Wang, Z. Jiang, X. Zhang, J. J. Zou, W. Mi, *Nat. Commun.*, 2020, **11**, 418.
- ³⁹ B. Fang, Z. Xing, W. Kong, Z. Li, W. Zhou, *Nano Energy*, 2022, **101**, 107616.
- ⁴⁰ Y. Liang, K. Banjac, K. Martin, N. Zigon, S. Lee, N.



- Vanthuyne, F. A. Garcés-Pineda, J. R. Galán-Mascarós, X. Hu, N. Avarvari, M. Lingenfelder, *Nat. Commun.*, 2022, **13**, 3356.
- ⁴¹ L. L. Hao, J. Y. Hu, J. Li, Y. J. Gao, Y. S. Meng, T. Liu, *ACS Catal.*, 2025, **15**, 5640-5650.
- ⁴² H. Li, Q. Quan, C. Y. Wong, J. C. Ho, *Adv. Energy. Sust. Rev.*, 2025, **6**, 2400326.
- ⁴³ E. Van der Minne, P. Vensaus, V. Ratovskii, S. Hariharan, J. Behrends, C. Franchini, J. Fransson, S. S. Dhesi, F. Gunkel, F. Gossing, G. Katsoukis, U. I. Kramm, M. Lingenfelder, Q. Lan, Y. V. Kolen'Ko, Y. Li, R. R. Mohan, J. McCord, L. Ni, E. Pavarini, R. Pentcheva, D. H. Waldeck, M. Verhage, A. Yu, Z. I. Xu, P. Torelli, S. Mauri, N. Avarvari, A. Bieberle-Huetter, C. Baeumer *Adv. Energy Mat.*, 2025, accepted | [ChemRxiv](#) | [Cambridge Open Engage](#).
- ⁴⁴ X. Chen, Y. Chen, Z. Shen, C. Song, P. Ji, N. Wang, D. Su, Y. Wang, G. Wang, L. Cui, *Appl. Surf. Sci.*, 2020, **529**, 147173.
- ⁴⁵ X. Sun, X. Liu, R. Liu, X. Sun, A. Li, W. Li, *Catal. Commun.*, 2020, **133**, 105826.
- ⁴⁶ X. Zou, Q. Lu, M. Tang, J. Wu, K. Zhang, W. Li, Y. Hu, X. Xu, X. Zhang, Z. Shao, L. An, *Nano-Micro Lett.*, 2025, **17**, 6.
- ⁴⁷ L. Jia, C. Wang, Y. Zhang, L. Yang, Y. Yan, *ACS Nano.*, 2020, **14**, 6607–6615.
- ⁴⁸ S. Mishra, A. Kumar, M. Venkatesan, L. Pigani, L. Pasquali, C. Fontanesi, *Small Methods*, 2020, **4**, 2000617.
- ⁴⁹ S. Mishra, E. G. Bowes, S. Majumder, J. A. Hollingsworth, H. Htoon, A. C. Jones, *ACS Nano*, 2024, **18**, 8663-8672.
- ⁵⁰ M. Al-Gharram, I. Jum'h, A. Telfah, M. Al-Hussein, *Colloids Surf. A*, 2021, **628**, 127342.
- ⁵¹ C. T. P. da Silva, V. L. Kupfer, G. R. da Silva, M. P. Moisés, M. A. G. Trindade, N. L. de Campos Domingues, A. W. Rinaldi, *Int. J. Electrochem. Sci.*, 2016, **11**, 5380-5394.
- ⁵² O. Belgherbi, D. Chouder, M. A. Saeed, *Optik*, 2018, **171**, 589-599.
- ⁵³ M. Al-Gharram, T. AlZoubi, *Ceram. Int.*, 2024, **50**, 5473-5482.
- ⁵⁴ K. Michaeli, V. Varade, R. Naaman, and D. H. Waldeck *J. Phys.: Condens. Matter* 2016, **29**, 103002
- ⁵⁵ A. Kumar, E. Capua, M. K. Kesharwani, J. M. L. Martin, E. Sitbon, D. H. Waldeck, and R. Naaman, *Proc. of the National Academy of Sciences* 2017, **114**, 2474.
- ⁵⁶ M. Eckshtain-Levi, E. Capua, S. Refaely-Abramson, S. Sarkar, Y. Gavrilov, S. P. Mathew, Y. Paltiel, Y. Levy, L. Kronik, R. Naaman *Nat. Comm.* 2016, **7**, 10744
- ⁵⁷ J. Lyskawa, D. Bélanger, *Chem. Mater.*, 2006, **18**, 4755-4763.
- ⁵⁸ W. Ullah, G. Herzog, N. Vilà, A. Walcarius, *Electrochem. Commun.*, 2021, **122**, 106896.
- ⁵⁹ N. F. Heinig, N. Kharbanda, M. R. Pynenburg, X. J. Zhou, G. A. Schultz, K. T. Leung, *Mater. Lett.*, 2008, **62**, 2285-2288.
- ⁶⁰ X. J. Zhou, A. J. Harmer, N. F. Heinig, K. T. Leung, *Langmuir.*, 2004, **20**, 5109-5113.
- ⁶¹ W. S. Huang, A. G. MacDiarmid, *Polymer*, 1993, **34**, 1833-1845.
- ⁶² R. Dubey, D. Dutta, P. Chattopadhyay, *Polym. Bull.*, 2024, **81**, 8547–8571.
- ⁶³ C. Clever, E. Wierzbinski, B. P. Bloom, Y. Lu, H. M. Grimm, S. R. Rao, W. S. Horne, D. H. Waldeck, *Isr. J. Chem.*, 2022, **62**, p.e202200045.
- ⁶⁴ B. P. Bloom, V. Kiran, V. Varade, R. Naaman, D. H. Waldeck, *Nano Lett.*, 2016, **16**, 4583-4589.
- ⁶⁵ F. Song, M. M. Busch, B. Lassalle-Kaiser, C. S. Hsu, E. Petkucheva, M. Bensimon, H. M. Chen, C. Corminboeuf, X. Hu, *ACS Cent. Sci.*, 2019, **5**, 558-568.
- ⁶⁶ M. Retuerto, L. Pascual, F. Calle-Vallejo, P. Ferrer, D. Gianolio, A. G. Pereira, Á. García, J. Torrero, M. T. Fernández-Díaz, P. Bencok, M. A. Peña, *Nat. Comm.*, 2019, **10**, 2041
- ⁶⁷ K. B. Ghosh, W. Zhang, F. Tassinari, Y. Mastai, O. Lidor-Shalev, R. Naaman, P. Mollers, D. Nurenberg, H. Zacharias, J. Wei, E. Wierzbinski, *J. Phys. Chem. C*, 2019, **123**, 3024-3031.
- ⁶⁸ L. F. Huang, M. J. Hutchison, R. J. Santucci Jr, J. R. Scully, J. M. Rondinelli, *J. Phys. Chem. C.*, 2017, **121**, 9782-9789.
- ⁶⁹ L. F. Huang, J. M. Rondinelli, *npj Mater. Degrad.*, 2019, **3**, 26.
- ⁷⁰ J. Chivot, L. Mendoza, C. Mansour, T. Pauporté, M. Cassir, *Corros. Sci.*, 2008, **50**, 62-69.
- ⁷¹ M. Bajdich, M. García-Mota, A. Vojvodic, J. K. Nørskov, A. T. Bell, *J. Am. Chem. Soc.*, 2013, **135**, 13521-13530.
- ⁷² W. Luo, C. Jiang, Y. Li, S. A. Shevlin, X. Han, K. Qiu, Y. Cheng, Z. Guo, W. Huang, J. Tang, *J. Mater. Chem. A*, 2017, **5**, 2021-2028.
- ⁷³ R. Swierk, S. Klaus, L. Trotochaud, A. T. Bell, T. D. J. Tilley, *J. Phys. Chem. C*, 2015, **119**, 19022-19029.
- ⁷⁴ S. Song, H. Bao, X. Lin, X. L. Du, J. Zhou, L. Zhang, N. Chen, J. Hu, J. Q. Wang, *J. Energy Chem.*, 2020, **42**, 5-10.
- ⁷⁵ X. Liu, S. Cui, Z. Sun, Y. Ren, X. Zhang, P. Du, *J. Phys. Chem. C*, 2016, **120**, 831-840.



- ⁷⁶ X. Liu, H. Jia, Z. Sun, H. Chen, P. Xu, P. Du, *Electrochem. Commun.*, 2014, **46**, 1-4.
- ⁷⁷ M. R. Gao, X. Cao, Q. Gao, Y. F. Xu, Y. R. Zheng, J. Jiang, S. H. Yu, *ACS Nano*, 2014, **8**, 3970-3978.
- ⁷⁸ M. Retuerto, L. Pascual, F. Calle-Vallejo, P. Ferrer, D. Gianolio, A. G. Pereira, Á. García, J. Torrero, M. T. Fernández-Díaz, P. Bencok, M. A. Peña, *Nat. Comm.*, 2019, **10**, 2041.
- ⁷⁹ X. Ren, T. Wu, Y. Sun, Y. Li, G. Xian, X. Liu, C. Shen, J. Gracia, H. J. Gao, H. Yang, Z. J. Xu, *Nat. Comm.*, 2021, **12**, 2608.
- ⁸⁰ T. Wu, Z. J. Xu, *Curr. Opin. Electrochem.*, 2021, **30**, 100804.
- ⁸¹ K. Shiota, A. Inui, Y. Hosaka, R. Amano, Y. Ōnuki, M. Hedo, T. Nakama, D. Hirobe, J. I. Ohe, J. I. Kishine, H. M. Yamamoto, *Phys. Rev. Lett.*, 2021, **127**, 126602.
- ⁸² H. Shishido, R. Sakai, Y. Hosaka, Y. Togawa, *Appl. Phys. Lett.*, 2021, **119**, 182403.



The data supporting this article has been included as part of the Supplementary Information.

